

Optical Engineering

SPIDigitalLibrary.org/oe

Calibration of the modulation transfer function of surface profilometers with binary pseudorandom test standards: expanding the application range to Fizeau interferometers and electron microscopes

Valeriy V. Yashchuk
Erik H. Anderson
Samuel K. Barber
Nathalie Bouet
Rossana Cambié
Raymond Conley
Wayne R. McKinney
Peter Z. Takacs
Dmitriy L. Voronov

Calibration of the modulation transfer function of surface profilometers with binary pseudorandom test standards: expanding the application range to Fizeau interferometers and electron microscopes

Valeriy V. Yashchuk

Lawrence Berkeley National Laboratory
Advanced Light Source
Berkeley, California 94720
E-mail: VVYashchuk@lbl.gov

Erik H. Anderson

Lawrence Berkeley National Laboratory
Center for X-Ray Optics
Berkeley, California 94720

Samuel K. Barber*

Lawrence Berkeley National Laboratory
Advanced Light Source
Berkeley, California 94720

Nathalie Bouet

Brookhaven National Laboratory
NSLS-II
Upton, New York 11973

Rossana Cambié

Lawrence Berkeley National Laboratory
Engineering Division
Berkeley, California 94720

Raymond Conley

Brookhaven National Laboratory
NSLS-II
Upton, New York 11973

Wayne R. McKinney

Lawrence Berkeley National Laboratory
Advanced Light Source
Berkeley, California 94720

Peter Z. Takacs

Brookhaven National Laboratory
Instrumentation Division
Upton, New York 11973

Dmitriy L. Voronov

Lawrence Berkeley National Laboratory
Advanced Light Source
Berkeley, California 94720

Abstract. A modulation transfer function (MTF) calibration method based on binary pseudorandom (BPR) gratings and arrays has been proven to be an effective MTF calibration method for interferometric microscopes and a scatterometer. Here we report on a further expansion of the application range of the method. We describe the MTF calibration of a 6 in. phase shifting Fizeau interferometer. Beyond providing a direct measurement of the interferometer's MTF, tests with a BPR array surface have revealed an asymmetry in the instrument's data processing algorithm that fundamentally limits its bandwidth. Moreover, the tests have illustrated the effects of the instrument's detrending and filtering procedures on power spectral density measurements. The details of the development of a BPR test sample suitable for calibration of scanning and transmission electron microscopes are also presented. Such a test sample is realized as a multilayer structure with the layer thicknesses of two materials corresponding to the BPR sequence. The investigations confirm the universal character of the method that makes it applicable to a large variety of metrology instrumentation with spatial wavelength bandwidths from a few nanometers to hundreds of millimeters. © 2011 Society of Photo-Optical Instrumentation Engineers (SPIE). [DOI: 10.1117/1.3622485]

Subject terms: surface metrology; binary pseudorandom; modulation transfer function; power spectral density; calibration; surface profilometer; interferometer; scanning electron microscope; transmission electron microscope.

Paper 110279PR received Mar. 21, 2011; revised manuscript received Jun. 27, 2011; accepted for publication Jul. 15, 2011; published online Sep. 1, 2011.

*Current address: University of California, Los Angeles, 40 Hilgard Avenue, Los Angeles, California 90095.

1 Introduction

In many applications, a statistical description of the surface topography via one-dimensional (1D) and two-dimensional (2D) power spectral density (PSD) distributions makes available rigorous experimental information about the expected

performance of the optic. The measured PSD distributions provide a closed set of data necessary for three-dimensional calculations of scattering of light by the optical surfaces.¹⁻⁴ Spectral analysis of the surface measurements is used to parameterize, specify, and model the topography of optical and engineering components⁵⁻⁸ as well as fabrication technologies, including optical polishing,⁹ lithography,¹⁰ surface coating, and multilayer (ML) deposition.^{11,12} Reliability of the PSD data for these and other applications relies on experimental methods available for comprehensive characterization and calibration of the metrology instruments in use.

In order to describe the spatial frequency response of imaging devices and surface profilometers, the concept of modulation transfer function (MTF) is widely used.¹³ The MTF of a profilometer accounts for the effects of the instrument's optical system, detector, signal processing, software algorithm, and environmental factors on the measured PSD distributions of the surface height and slope (see, e.g., Refs. 14-19 and references therein).

In the course of PSD measurements of a surface under test (SUT) with pixel dimensions Δx and Δy and M and N number of pixels in the tangential and sagittal directions, respectively, the measured surface 2D PSD, $\text{PSD}_{\text{measured}}$, is obtained by the square modulus of a straightforward discrete Fourier transform of the measured height distribution $h_{m,n}$.¹⁷⁻¹⁹

$$\text{PSD}_{\text{measured}}(l, k) = M N \Delta x \Delta y |F_{l,k}|^2, \quad (1)$$

where $F_{l,k}$ are the elements of the Fourier transform matrix,

$$F_{l,k} = \frac{1}{M} \sum_{m=0}^{M-1} \left[\exp\left(\frac{-2\pi i m l}{M}\right) \frac{1}{N} \sum_{n=0}^{N-1} h_{m,n} \exp\left(\frac{-2\pi i n k}{N}\right) \right]. \quad (2)$$

The corresponding estimates of the tangential and sagittal 1D two-sided PSD $S'_1(l)$ and $S'_1(k)$ can be obtained by summing over rows (l) or columns (k), respectively. Here $0 \leq l \leq M-1$ and $0 \leq k \leq N-1$, and prime signifies a two-sided PSD. These are then converted to one-sided (positive frequency only) just like the ones calculated from lines on the surface directly

$$S_1(l) = 2S'_1(l)g(l) \text{ and } S_1(k) = 2S'_1(k)g(k), \quad (3)$$

where $0 \leq l \leq M/2$, $0 \leq k \leq N/2$; $g(l) = 1/2$ at $l = 0, M/2$, $g(k) = 1/2$ at $k = 0, N/2$, and $g(l) = 1$ and $g(k) = 1$ otherwise.

To the extent that the response of the instrument can be characterized as a linear system, the measured PSD is a product of the PSD inherent for the SUT, PSD_{SUT} , and the MTFs of the individual components (objective, detector, etc.) of the instrument:

$$\text{PSD}_{\text{measured}} = \text{PSD}_{\text{SUT}} \times \text{MTF}^2. \quad (4)$$

The MTF in Eq. (4) is the total MTF of the instrument. It can be experimentally determined by comparing the measured PSD distribution of a test surface to the corresponding ideal PSD distribution, which is numerically simulated or found from PSD measurements with an instrument with significantly higher resolution. The square root of the ratio of the measured PSD distribution to the ideal PSD distribution gives the MTF of the instrument.

A number of methods for MTF measurement have been developed.²⁰⁻³³ The effectiveness of a given method hinges critically on the appropriate choice of test surface. A successful test surface should be suitable for calibration over the entire instrumental field of view with a uniform sensitivity to the MTF over the entire spatial frequency range up to the Nyquist frequency of the instrument. Additionally, in order to be used as a certified standard, the MTF test surface should satisfy the conditions of ease of specification, reproducibility, and repeatability; and the accuracy of the MTF calibration should have a reasonably low sensitivity to possible fabrication imperfections of the surface. Most of the common test patterns used in MTF measurements, including knife-edge sources (step height standards),²⁰⁻²⁴ bar targets,²⁵ sinusoidal surfaces,²⁶ periodic and quasiperiodic patterns,²⁷⁻³⁰ white noise patterns,³¹ and random reference specimens^{28,32} fail to meet all of these requirements. For a comprehensive review of standard reference specimens, see Ref. 33 and references therein.

Recently, an original technique for precise measurement of the 1D and 2D MTFs has been developed. The technique is based on the use of binary pseudorandom gratings and arrays (BPRA).^{34,35} Unlike most conventional test surfaces, the inherent PSD of the binary pseudorandom (BPR) gratings and arrays has a deterministic white-noise-like character. This allows the direct determination of the 1D and 2D MTFs, respectively, with a sensitivity uniform over the entire spatial frequency range of a profiler. The success of applying this method to different interferometric microscopes and a scatterometer has been experimentally demonstrated.³⁴⁻³⁹

In Sec. 3, we extend the BPRA method to large field-of-view interferometers, a class of instruments that are, and we believe will continue to be, a standard for making high precision surface height measurements over relatively low spatial frequency ranges from approximately 10^{-2} to 10 mm^{-1} . In this case, a 2D BPRA test sample of 4027×4029 elements with fundamental element size of $20 \mu\text{m}$ and height of 100 nm was fabricated by a conventional microlithography technique. The fundamental element size was chosen to be a few times smaller than the highest lateral resolution possible with the ZYGO GPITM interferometer under test.

An extension of the method to the micro- and nanoscale measurements with scanning and transmission electron microscopes (SEM and TEM, respectively) is presented in Sec. 4. The test samples suitable for calibration of electron microscopes are made of the BPR multilayer (BPRM) structures with a focused ion beam technique. The BPRM samples of two materials are seen as 1D BPR structures of different contrast when observed with an electron microscope. The fundamental layer thickness of 3 nm and the overall thickness of the multilayer cross-section of about $6 \mu\text{m}$ determine the spatial frequency range available for calibration with the samples.

Besides the significant, by many orders of magnitude, extension of the spatial frequency range of applicability of the method (to both lower and higher frequencies compared to that of the previous work with interferometric microscopes and visual-light scatterometer³⁴⁻³⁹), we demonstrate here the universal character of the used approach, suitable to characterize these principally different instruments. Universality is ensured by the similarity of specification of the test samples as sets (1D gratings and sequences, or 2D arrays) of pseudorandomly distributed elements with a binary

(two-level) physical property such as two height levels or two materials with different contrast.

This paper is organized as follows. In Sec. 2, we briefly overview the mathematical fundamentals of BPR sequences and arrays that are important for MTF measurements. Section 3 discusses the development of the first prototype BPR test surfaces suitable for MTF measurements with large aperture interferometers. Specifically, we present the results of MTF tests with a ZygoTM-GPI 6-in. Fizeau interferometer. The details of fabrication and use of a BPR multilayer structure, suitable for characterization of SEMs and TEMs, are presented in Sec. 4. The paper concludes (Sec. 5) by summarizing the main concepts discussed throughout the paper and stating a plan for extending the technique to calibrate other types of surface profilometers, including scanning probe (atomic force) microscopes. The investigations confirm the universal character of the method that makes it applicable to a large variety of metrology instrumentation with spatial wavelength bandwidths from a few nanometers to hundreds of millimeters.

2 BPR Sequences and Arrays

BPR sequences and arrays are one- and two-dimensional patterns, respectively, of statistically independent and uniformly distributed binary elements (1's and 0's or -1 's and $+1$'s). We use the term "pseudorandom" to emphasize that the distributions are generated by mathematically precise rules to be random in the mathematical strong sense.^{40–42} Alternatively, such sequences are referred to in literature as pseudonoise sequences or m -sequences.⁴⁰

Particular methods for generation of pseudorandom sequences^{43,44} were developed in connection with communication and encryption processes,⁴⁵ acoustics,⁴⁶ and pseudorandom chopping of a beam in time-of-flight experiments with slow neutrons^{47–52} and molecular beams.^{53–55} The maximum duty cycle (relative number of 1's and 0's) of approximately 50% is obtained with a maximum-length pseudorandom sequence (MLPRS).^{44,53,54} A sequence $\{a_i\}$ of N elements, $i = 0, 1, \dots, N - 1$, $N = 2^n - 1$, where n is an integer, is qualified as a MLPRS, if i. the autocorrelation of the sequence sums to 2^{n-1} and ii. the sequence is "almost" uncorrelated. The conditions i. and ii. are very natural for a purely random sequence, or white noise that consists entirely of uncorrelated binary elements with a delta-function-like correlation function. According to the Wiener–Khinchin theorem,⁵⁶ the PSD of a sequence with a delta-function-like correlation function is a frequency independent white-noise-

like distribution. The 1D BPR sequences used in this publication were generated using the algorithm described in detail in Ref. 44.

Two-dimensional analogues to 1D BPR sequences are designated as uniformly redundant arrays (URAs). URAs are widely used as optimal mask patterns for coded aperture imaging techniques.⁴¹ Analogous to the time-of-flight technique based on 1D BPR sequence chopping,^{47–55} an imaging technique based on the 2D URAs allows one to obtain a better signal-to-noise ratio, keeping the high angular resolution characteristic of a single pinhole aperture.^{57–59} Similar to 1D BPR sequences, the URAs possess both high throughput (50%) and a delta-function-like cyclical autocorrelation function that corresponds to a flat 2D PSD spectrum. Due to the similarity, we employ the term BPR array rather than URA, when discussing the 2D test surfaces used for the MTF calibration. The URA used in this paper follows the original prescription of the twin-prime class given in Ref. 57. The URA is configured as a rectangular aperture of dimensions $r \times s$, where r and s are prime numbers and $r = s + 2$. For more details on the URA generation algorithm see Refs. 57 and 58.

1D and 2D BPR gratings and arrays which we use for MTF calibration of surface profilometers (such as interferometric microscopes,^{34–39} scatterometers,³⁷ and, now, large area interferometers), are sets of rectangular grooves pseudorandomly distributed over a uniform 1D and 2D grid, respectively.

Figure 1(a) illustrates the design of a BPR array. The pitch of the grid (width of the smallest element of the pattern), Δ , determines the inherent Nyquist frequency of the BPR pattern, $f_N = 1/2\Delta$. For lower spatial frequencies, the inherent PSD is limited by the whole size of the array, $r\Delta$ and $s\Delta$ for the two orthogonal directions, $f_{Lx} = 1/r\Delta$ and $f_{Ly} = 1/s\Delta$, respectively. The height of the pattern, h_0 , determines the amplitude of the array's inherent PSD spectrum. Because the PSD from a BPR grating or array is a result of the groove distribution, it is not particularly sensitive to the groove shape or roughness of the groove surfaces, top or bottom.^{38,39} The only requirement is that the value of h_0 should be large enough to ensure a negligible contribution from fabrication imperfections to the PSD measurements.

Figure 1(b) illustrates a design of a BPR ML test sample suitable for measurements with electron microscopes. A BPRML sample is a multilayer structure consisting of two materials (marked with indexes 0 and 1) with significantly different contrast when observed with an electron

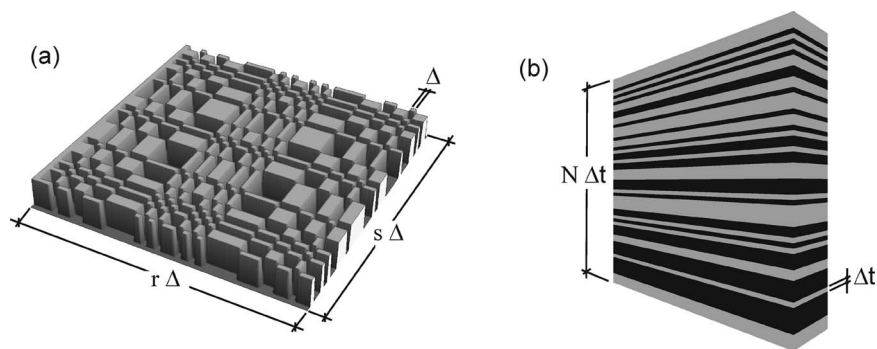


Fig. 1 Examples of BPR test patterns: (a) 2D BPR array of 43×41 elements; (b) BPR multilayer consisting of 63 elementary sub-layers of thickness Δt . In order to generate the BPR patterns, the algorithms described in Refs. 44 and 57 were used.

microscope. In order to serve as a test sample for MTF calibration of a SEM or a TEM, the layers of the two materials are pseudorandomly distributed according to a binary pseudorandom sequence, similar to ones used for fabrication of BPR gratings and applied to 1D MTF calibration of interferometric microscopes.^{34,35} In the BPRML case, the thickness of a particular layer of the material with index 0 (1) is equal to the elementary thickness of the multilayer, Δt , multiplied by the number of adjacent 0's (1's) in the BPR sequence used for the multilayer generation.

The BPR array and grating patterns used throughout the present work are generated with a maximum filling factor of about 50% providing an improved signal-to-noise ratio of the PSD spectra of the test surface. The inherent PSD spectrum of such a pattern is independent of spatial frequency (white-noise-like). Therefore, any deviation of a PSD spectrum measured with a real instrument from a white-noise-like spectrum is a measure of the instrumental MTF.

3 BPR Array Sample for Use With Large Aperture Interferometers

3.1 BPR Array Fabrication

Due to their deterministic binary character, BPR test surfaces are easy to specify for standard micro- and nanofabrication processes. For the purpose of MTF measurement, an ideal surface based on a BPR pattern is determined as a set of rectangular grooves of binary height levels with grooves and peaks corresponding to values of 1 and 0 in the BPR sequence or array [Fig. 1(a)]. The optimal height, h_0 , and fundamental element size (pitch), Δ , depend on the specifics of the instrument under calibration.³⁷

In order to carry out MTF calibration of an interferometer, an optimal BPR sample should have i. a fundamental element size smaller than the highest lateral resolution available with the instrument; ii. the height step should be smaller than the light wavelength, $h_0 < \lambda$, and iii. the test pattern should fill a relatively large area of the instrumental field of view.

In the case of the 6-in ZygoTM-GPI interferometer under test, the lateral resolution can be varied from about 0.4 mm down to approximately 0.09 mm depending on the optical magnification. Therefore, for an adequate BPR test sample according to condition i., we choose a fundamental element size of 20 μm that provides a sufficient higher spatial frequency bound.

Conditions ii. and iii. lead to a relatively stringent requirement that the figure error of the BPR substrate be less than $\lambda/20$ over a clear aperture of about 150 mm. In addition to the high price of such substrates, they are also rather thick, 3/4 to 1 in., making it difficult to use them in conventional microlithography machines and processes. For this reason, the first prototype BPR samples (with 4027×4029 elements with 20- μm fundamental element size) for MTF calibration of the ZygoTM-GPI interferometer were fabricated by conventional microlithography with chromium deposition on a standard 4 in. silicon wafer with a thickness of 4 mm.

Figure 2(a) shows the higher spatial frequency topography of a 1.25 mm \times 0.94 mm sub-area of a total 80.54 mm \times 80.58 mm pattern of the fabricated BPR array as it was seen with the MicroMapTM-570 interferometric microscope equipped with a 10 \times objective. The resolution of the microscope ($\sim 2 \mu\text{m}$) is adequate for examination of the quality of the profile of the BPR elements obtained with the used microlithography process. Based on the consideration of the effect of the BPR fabrication imperfections on the MTF correction given in Refs. 38 and 39, we conclude that the observed irregularity of the profile of the array elements is negligible, perturbing the inherent BPR PSD distribution at higher spatial frequencies by less than 1%. The BPR's geometrical parameters were measured with an atomic force microscope to be $h_0 \cong 100 \text{ nm}$ and $\Delta \cong 20 \mu\text{m}$, exactly as desired.

As it was expected with a low budget substrate used for fabrication of the BPR, the residual curvature and low frequency variations of the wafer are significantly worse than that which is required for an ideal substrate, $\ll h_0$, according to condition ii. above. Measurements with the ZygoTM-GPI with 1 \times magnification [Fig. (2)] revealed that the fabricated BPR test surface has a curvature on the order of 1000 m, which masks the appearance of the BPR features, even at a larger magnification of the interferometer. The measured peak-to-valley variation of $\sim 5 \mu\text{m}$ is much larger than the BPR height $h_0 \cong 100 \text{ nm}$.

Note that a similar problem was encountered during the calibration of the MicroMapTM-570 interferometric microscope when using the smaller magnifications, e.g., 2.5 and 5 \times objectives.^{37,38} In these cases, waviness of the substrate tended to distort the measured PSDs from the PSDs expected to result from the mathematical properties of the BPR. The solution to this problem was to etch the BPRs into a superpolished silicon substrate. Because the largest field of

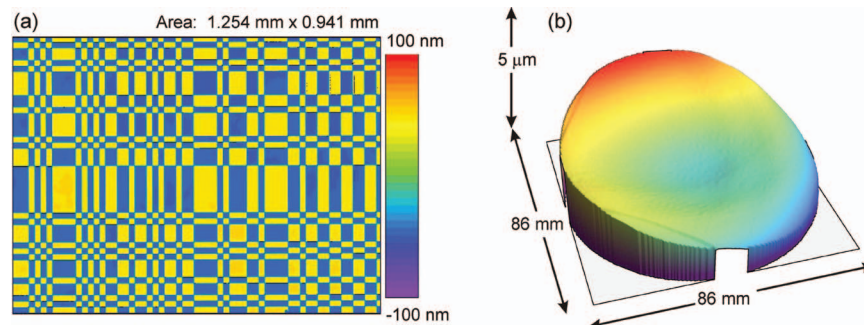


Fig. 2 (a) Height distribution measurement over 1.25 mm \times 0.94 mm sub-area of the developed BPR test sample performed with the MicroMapTM-570 interferometric microscope equipped with a 10 \times objective. (b) Measurement of the BPR sample height distribution over the entire area with a ZygoTM-GPI with the 1 \times magnification. The BPR surface structure is almost invisible due to the figure (low spatial frequency) variation of the sample's surface.

view with the MicroMapTM-570 microscope is only 2.51 mm \times 1.88 mm, a suitable substrate is relatively inexpensive, and the corresponding developments are currently in progress at the Advanced Light Source Optical Metrology Laboratory.

In the case of the ZygoTM-GPI, two mutually supplemental alternatives to starting with a BPRa test sample on an excessively expensive substrate have been employed. First, the overall lower spatial frequency variations of the substrate could be accurately fitted and subtracted using Zernike polynomials or filtered out with the Zygo software's data filtering options. An ideal fitting/filtering procedure would remove all low frequency irregularities without disturbing the higher spatial frequency structure of the measured PSD spectra. Second, the range of substrate figure variations can be significantly decreased if the MTF calibration is applied to the ZygoTM-GPI interferometer with the maximum magnification (nominally 6 \times). Such proof-of-principle MTF measurements are the focus of the present work (see Sec. 3.2).

3.2 MTF Measurements with ZygoTM-GPI Interferometer

The BPRa test sample was mounted in the front of the ZygoTM-GPI interferometer on a rotatable kinematic mount and visually aligned to the grid of the interferometer's CCD. The small value of the fundamental period of the BPRa (20 μ m) allows for the measurement of the MTF of the ZygoTM-GPI with maximum magnification, i.e., when the nominal pixel size of the CCD detector is about 90 μ m. However, even at the maximum magnification, the BPRa surface figure measured over the whole field of view (640 \times 480 pixels) still exhibits significant low frequency variations. Neither detrending with the Zernike polynomials or astigmatic (cylindrical) surfaces, nor using a fast Fourier transform (FFT) filter with a low frequency cutoff, available in the Zygo software, fully removed these variations.

Nevertheless, Zygo MTF tests were still possible using a reduced field of view of approximately 215 \times 215 CCD pixels (a 19.4 mm \times 19.4 mm area) and measuring the central portion of the test surface, which had the least amount of curvature. The data were then filtered using a FFT filter, available with the Zygo MetroPro Version 7.6.1 software, with three different low frequency cutoffs of 0.025, 0.25, and 0.5 mm^{-1} . Note that when filtering of this type is used, the size of the data set is necessarily reduced because points along the perimeter of the field of view are excluded by the Zygo software.

Figure 3 depicts 2D height distribution measured with the 6-in aperture ZygoTM-GPI under test over 19.4 mm

\times 19.4 mm sub-area of the BPRa sample developed and shown with higher resolution in Fig. 2(a) as measured with the MicroMapTM-570 interferometric microscope. The different plots in Fig. 3 are presented to visualize the effects of filtering the data compared with detrending with the best fitted astigmatic (cylindrical) surface. Detrending removes a significant amount of the substrate's saddle like shape, but filtering clearly provides a better means for removing other low frequency variations.

Throughout the present work, the recorded surface height distributions (as well as the SEM and TEM intensity distributions) are transformed to 2D PSD distributions by using the calculation procedure described in detail in Refs. 17–19, and briefly outlined in Sec. 1. The corresponding 1D PSDs are obtained by a direct integration (discrete summing) of the 2D PSDs. No additional filter or windowing to the data (except the filters with the Zygo software described above) is used for the PSD calculation.

A comparison of the PSDs from the unprocessed data, the detrended data, and the filtered data indicates positive results, Fig. 4. Both the tangential and sagittal PSDs before detrending or filtering demonstrate an inverse-power-like (a negative slope on a log–log scale) character. Detrending the data significantly reduces the PSD level at the lower spatial frequencies, but there is still a significantly raised lower frequency tail. As filtering is applied with increasing cutoff frequency, however, the raised low frequency tail starts to flatten out and the PSDs start to exhibit precisely the expected characteristics for a BPRa test surface. That is, the PSD is largely flat across the lower frequency range before it begins to roll off in the higher frequency range, which is primarily an effect of the instrumental MTF. Note that the low frequency filtering does not cause any noticeable perturbations to the PSD at the higher frequency range (limited by the roll-off at the Nyquist frequency), interesting from the point of view of MTF measurement. Thus, FFT filtering is a suitable method for removing inherent waviness of the substrate and recovering the desired BPRa height distribution, which can then be used for MTF calibration.

The major result from the ZygoTM-GPI MTF measurements is that the instrument's Nyquist frequencies, easily identified by visual inspection of the 1D PSDs, in the tangential and sagittal directions are significantly different. To determine the source of this asymmetry, the BPRa test surface was rotated 90° from its original orientation and re-measured. Comparison of the measurements with and without rotation has confirmed that the asymmetry is inherent to the Zygo MetroPro Version 7.6.1 software that processes the data from rows and columns of the CCD in different ways. Note that a similar asymmetry of the tangential and

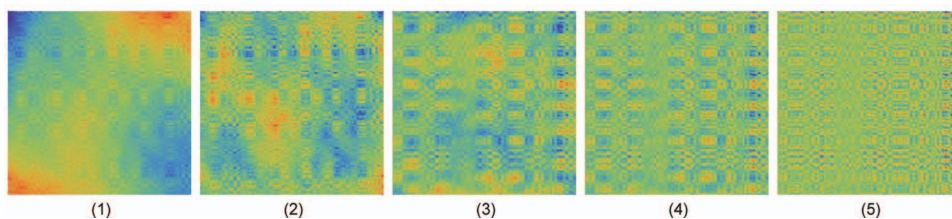


Fig. 3 Two-dimensional height distribution plots of the BPRa measured with a Zygo 6-in. Fizeau interferometer equipped with the nominal 6 \times magnification over 19.4 mm \times 19.4 mm sub-area of the BPRa sample developed. (1) No filtering or detrending applied; (2) detrended with the best fit astigmatic (cylindrical) surface; (3), (4), and (5) data filtered using an FFT filter with low frequency cutoffs of 0.025, 0.25, and 0.5 mm^{-1} , respectively.

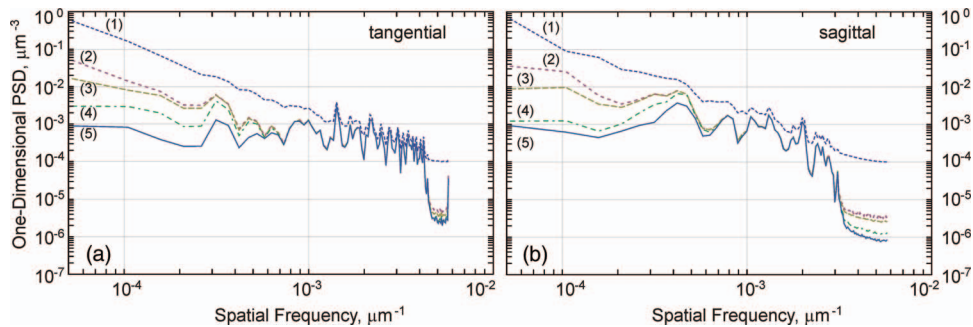


Fig. 4 One-dimensional PSDs obtained from BPR test sample height distribution measured with a Zygo 6-in. Fizeau interferometer equipped with the nominal $6\times$ magnification. (1) No filtering or detrending applied; (2) detrended with the best fit astigmatic (cylindrical) surface; (3), (4) and (5) data filtered using an FFT filter with low frequency cutoffs of 0.025, 0.25, and 0.5 mm^{-1} , respectively.

sagittal PSD spectra has also been observed with another phase measuring Fizeau-type interferometer.⁵⁹

The observed asymmetry is remarkably analogous to a discovery regarding how the MicroMapTM-570 processes data.^{17,19} In the case of the MicroMapTM-570, a detailed investigation of the origin of the anisotropy problem has been performed.¹⁷ The problem appears when a two field interlaced camera is used.⁶⁰ One field consists of odd pixel lines, another includes the even lines. Both fields are collected simultaneously but are read out alternately. Such a read-out process leads to a systematic distortion between alternate detector outputs, corresponding to two fields. This distortion is reduced by averaging (summing) alternate outputs with the instrumental software. The averaging eliminates the distortion but also reduces the image resolution (Nyquist frequency) in the sagittal direction, and, therefore, the spatial frequency bandwidth of the instrument. Note that in the case of the MicroMapTM-570, the latest (fifth) version of the microscope software accounts for the asymmetry by applying an additional averaging over two neighboring columns.

4 BPR Multilayer Test Samples for Use With Electron Microscopes

We consciously include in the present article the current section that describes the MTF calibration method applicable to electron microscopes. This method seems to be, on first glance, significantly different from the method used to measure MTF of a large aperture optical interferometer discussed above. Nevertheless, even in spite of the facts that the instruments are principally different and the MTF test samples do not look similar and are made using absolutely different technology, the basic principle of the calibration stays the same. That is, the use of the binary pseudorandom test pattern with a deterministic white-noise-like inherent PSD spectrum. Such similarity between the applications is a demonstration of deep universality of the calibration method that can be also extended to other metrology instrumentation of different operational principles, e.g., atomic force microscopes.

An extension of the method to the micro- and nanoscale measurements with SEM and TEM is presented in this section. The test samples suitable for calibration of electron microscopes are made of the BPRM structures with a focused ion beam technique. The BPRM samples of two materials are seen as 1D BPR structures of different contrast when observed with an electron microscope. The fundamental layer thickness of 3 nm and the overall thickness of the multilayer

cross-section of about $6\text{ }\mu\text{m}$ determine the spatial frequency range available for calibration with the samples.

As pointed out in Sec. 2, a test sample suitable for measurements with electron microscopes can be made of the BPR multilayer structure consisting of two materials with significantly different contrast [Fig. 1(b)]. In this case, the layers of the two materials are pseudorandomly distributed according to a binary pseudo-random sequence, similar to ones used for fabrication of BPR gratings and applied to 1D MTF calibration of interferometric microscopes.^{34,35}

Below we provide the details of fabrication of such BPRML test samples (Sec. 4.1) and the first results from use of such samples to characterize metrology performance of SEM (Sec. 4.2) and TEM (Sec. 4.3) instruments.

4.1 Fabrication of BPR Multilayer Test Samples

Here we describe the details of the development of BPRML test samples suitable for measurements with scanning and transmission electron microscopes. First, we create a multilayer structure consisting of two materials, WSi_2 and Si (marked with indexes 0 and 1, respectively) with significantly different contrasts when observed with an electron microscope. In order to serve as a test sample for MTF calibration of an SEM or TEM, the 1010 layers of the two materials have thicknesses pseudorandomly distributed according to a binary pseudorandom sequence of 2047 total elements. The thickness of a particular layer of the material with index 0 (1) is equal to the elementary thickness of the multilayer, $\Delta t = 3\text{ nm}$, multiplied by the number of adjacent 0's (1's) in the BPR sequence used for the multilayer generation. The thickest deposited layer in the stack is 33 nm, which corresponds to 11 of the same (0's or 1's) adjacent elements. The specified total thickness of the multilayer deposited is 6141 nm. The first layer of 33 nm of WSi_2 is on the substrate, while the top layer of 6 nm of Si is exposed to air. The overall size of the sample multilayer deposited on 0.5-mm thick Si (100) substrate is approximately $25\text{ mm} \times 12.5\text{ mm}$.

The BPR sequence of 2047 elements was generated using parameters⁴⁴ $n = 11$ and $M = 83$. Unfortunately, the recursion coefficient $M = 83$ was used mistakenly (instead of $M = 43$); it does not correspond to a recursion coefficient which produces an ideal MLPRS. Although the fabricated BPRML samples do not correspond to an ideal BPR distribution, the samples were found to be still suitable for MTF measurements with an SEM. As verified analytically, the autocorrelation function of the sequence is very close to a

one-element delta-function expected for the corresponding BPR sequence (e.g., with $M = 43$); and the inherent PSD spectrum is a white noise one, however, with a noticeable level of noise. A new BPR multilayer with the ideal BPR distribution of layers and with even smaller elementary thickness (1.5 nm) and larger total number of elementary layers (4095) is in progress.

The BPR multilayer was fabricated with solid-source targets of B-doped Si and hot-pressed WSi_2 using modified 3-in. direct-gas injection cathodes⁶¹ in a turbopumped rotary deposition system. The target to sample distance was 78 mm, with a process gas pressure of Ar held at a constant 2.3 MT by an upstream dual-MFC feedback control. The average gas flow through each cathode was ~ 9 SCCM. Deposition was carried out at a constant power of 170 W for both guns. The proper thickness for each individual layer is produced by raster-scanning the substrate over figured apertures by varying both the number of passes over this aperture and the rotational velocity. Due to the inherent nature of the magnetron deposition growth rate to decay over time, a compensation factor is included during the growth, which adjusts the velocity appropriately as is used for growth of other types of thick multilayers.^{62,63}

Test sample preparation and the SEM and TEM measurements with the samples were performed at Evans Analytical Group, Inc.⁶⁴ The BPRMLs were loaded in and processed with a Dual Beam FIB (focused ion beam)/SEM instrument (Helios NanoLab,TM FEI Company). The instrument integrates imaging capabilities of a field emission SEM and the capability for preparation of a precise thin sample cross-section using a focused ion beam. In order to avoid rounding of the top surface edge of the sample cross section in the course of FIB etching, the area of the BPRML used for the SEM measurements was preliminary coated with a thin, about 1.5- μm thick, layer of Pt.

For the SEM measurements, the BPRML was cross-sectioned by etching with the FIB/SEM technique — Fig. 5(a). After careful FIB flattening of the side wall of the dimple shown in Fig. 5(a), the dissected BPR multilayer cross-section was measured with a SEM — Sec. 4.2.

The process for fabrication of a test sample suitable for measurements with a TEM consisted in FIB etching out of a thin sample from the BPRML — Figs. 4(a) and 5(b). The TEM sample preparation was performed with the multilayer piece shown in Fig. 5(b) when it was completely detached from the multilayer. In this step, in order to hold the piece, a sharp transporting needle was Pt ion-beam welded to the free, right-hand side of the piece. After that, the piece was

cut out from the rest of the BPRML and attached to a pin of a standard TEM sample holder, Fig. 5(c). Finally, in order to decrease the test sample piece thickness to ~ 60 to 100 nm and make the thickness uniform, both sides of the ML piece at its free end were processed with “super-polishing” at extremely low FIB current.

Figure 5(c) shows an SEM image of the BPRML TEM sample prepared using the FIB/SEM process described above. Because SEM imaging is associated with a noticeable ablation of the sample material, the last SEM measurement was carried out just before the last cycle of the FIB “super-polishing.” After the FIB/SEM preparation of the BPRML TEM sample was completed, the FIB/SEM vacuum chamber was vented and the holder with the sample was moved to a clean glass dish. In this way the sample was brought to a TEM lab.

4.2 SEM Measurements of the BPRML Cross-Section

SEM measurements of the multilayer cross section [Fig. 5(a)] prepared with the FIB technique were performed with an electron beam tilted by 52° with respect to the surface normal. This led to a distortion of the vertical scale of the SEM photomicrograph of the cross sections of the samples. The distortion should be accounted for when estimating the thickness of the layers and calculating the PSD spectra. Figure 6(a) shows an SEM image of a cross-section of the BPRML sample obtained with $35,000\times$ magnification. The vertical bar in the image is placed in order to provide a corrected vertical scale that accounts for the 52° tilt of the electron beam.

Magnification of $35,000\times$ is suitable for acquiring an image of the entire ML cross-section; however, it is too low to resolve the thinnest layers of the BPRML structure. SEM images of the BPRML samples measured with a significantly increased magnification ($200,000\times$) are shown in Fig. 6(b). It still seems that magnification of $200,000\times$ is not enough to resolve the thinnest layers of the BPRML structure. Images with significantly higher resolution were obtained using FIB/TEM technology (Sec. 4.3).

As an example of the valuable information that can be obtained with the developed BPRML test samples, in Fig. 6(c) we show how the measurements of the BPRML lead to understanding of the limitations of FIB/SEM analysis. Figure 6(c) presents 1D PSDs calculated for the “top third,” (dashed line), “middle third” (dashed-dotted line), and “bottom third” (solid line) of the BPRML image

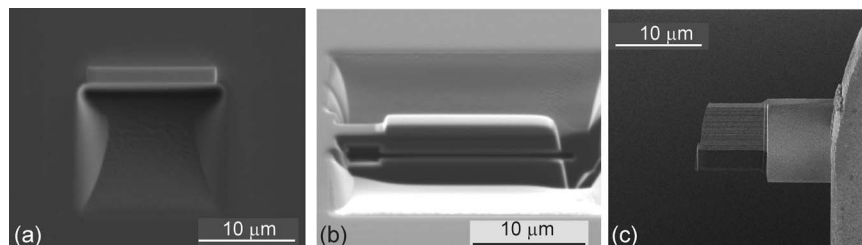


Fig. 5 (a) Photomicrograph of the BPRML with a dimple etched with the FIB. In the course of FIB etching, deposition of the etched material leads to overgrowth of the sides of the dimple. The sample was used for SEM measurements discussed in Sec. 4.2. (b) Photomicrograph of the BPRML with sample multilayer section detached from the Si substrate by FIB etching and undercutting across the Si substrate cross-section. The sample was used for TEM measurements discussed in Sec. 4.3. (c) Photomicrograph of the multilayer test sample piece under super-polishing to approximate 80-nm thickness suitable for TEM imaging.

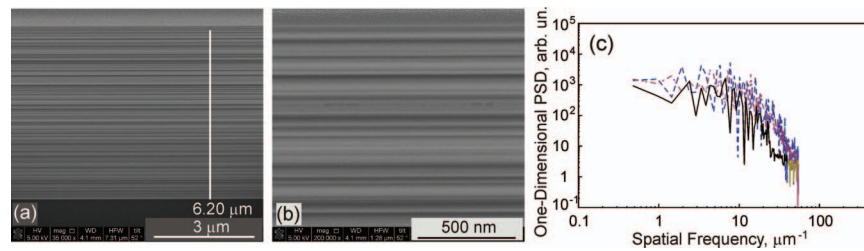


Fig. 6 (a) SEM image of a cross section of the BPRML [see Fig. 5(a)] obtained with $35,000\times$ magnification. (b) SEM image of a cross section of the BPRML obtained with $200,000\times$ magnification. (c) Power spectral densities calculated for the top third (blue dashed line), middle third (red dashed-dotted line), and bottom third (black solid line) of the image shown in (a). The defocusing effect is clearly seen as a lower spatial frequency shift of the PSD spectra for the bottom third part of the image. (Color online only.)

obtained with $35,000\times$ magnification [Fig. 6(a)]. The observed differences of the spectra suggest that the SEM images performed at a tilt angle of 52° suffer from a limited focal depth of the instrument. As a result, for a vertically lengthy sample, such as our BPRML cross-section, the image resolution varies significantly in the vertical direction.

In order to obtain PSD distributions from the SEM measurements [Fig. 6(c)], the images in tiff-format [as ones shown in Figs. 6(a) and 6(b)] were analyzed by converting the image brightness profiles to 1D PSD distributions. We used the following PSD processing. First, in order to avoid a contribution to the PSD spectrum from a gate-like function associated with the averaged image brightness, an original 2D brightness distribution was detrended by subtracting the best fitted plane surface. As a result, the averaged brightness of the detrended image is equal to zero (a negative brightness value is now allowed). Second, after detrending, 1D PSD distributions were calculated for each column and averaged to decrease random spectral variation in the way described, e.g., in Refs. 17–19. The PSD spectra at this stage have a characteristic high frequency roll-off that is due to the limited resolution of the SEM. The spectra flatten at significantly high frequencies where a contribution of the instrumental random noise exceeds the PSD magnitude inherent to the image of the structure. Finally, the random noise spectrum is removed by subtracting a minimum PSD value of the flat tail. In this way, we avoid obtaining a negative PSD value that is unphysical.

4.3 TEM Measurements with the BPRML Sample Prepared with SEM/FIB Technique

The structure of the BPRML TEM sample was investigated with a Tecnai™ TEM instrument (FEI, Co.). The instrument is capable of high-resolution transmission electron and

scanning transmission electron microscopy. With electron energies of about 300 keV and with ultrathin samples, the TEM image resolution is on the order of 1 to 2 Å. Compared to SEM, the TEM has better spatial resolution, and is capable of additional analytical measurements, but requires significantly more sample preparation, as described above.

Figure 7 shows the TEM images of the BPRML sample piece [Fig. 5(c)] obtained with different magnifications. The resolution of the image, obtained at a rather low electron energy of 2.3 keV [Fig. 7(a)], is noticeably higher than that of the image obtained with the SEM and shown in Fig. 6(a). There is a noticeable contrast variation from top to bottom of the image that is due to the variation of the sample thickness. The contrast variation of a TEM image can be significantly improved by detrending the image with a 2D low order polynomial distribution. The specified relative accuracy of distance measurements with the SEM and TEM is 2% to 3%. This can explain the difference of the thickness values obtained with the instruments [compare the scale lines in Figs. 6(a) and 7(a)]. Note that in the TEM images we do not see any noticeable imperfection of the multilayer structure. This is in contrast to a few of the measurements with the SEM in which we saw waviness in the layers.

The measurement in Fig. 7(b) was performed at an electron energy of 17.5 keV. The corresponding resolution is high enough to provide high contrast separation, even for the thinnest layers with 3-nm thickness. High resolution (at 255 keV electron energy) TEM measurements of the BPRML test sample are shown in Figs. 7(c) and 7(d). The TEM resolution is about 2 Å, allowing for the observation of the interlayers of the ML coating. Moreover, in Fig. 7(c) an amorphous layer of Pt deposition is visible on the top of the sample, and a layer of oxidized Si is clearly seen on the top of the Si substrate [bottom of Fig. 7(d)]. Note the very high contrast between the WSi_2 and Si layers. The observed

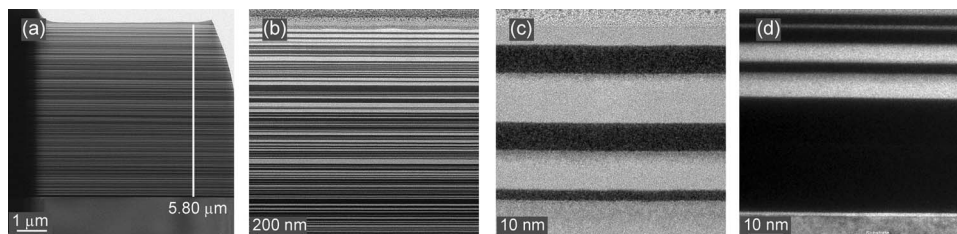


Fig. 7 (a) TEM images of a cross section of the BPRML sample piece obtained: at an electron energy of (a) 2.3 keV, (b) 17.5 keV, and (c) and (d) 255 keV. The contrast variation from top to bottom of the low magnification image (a) is due to the variation of the sample thickness. The images in (b) and (c) were taken over areas at the top of the BPRML test sample. The image in (d) approximately corresponds to the bottom part of the sample.

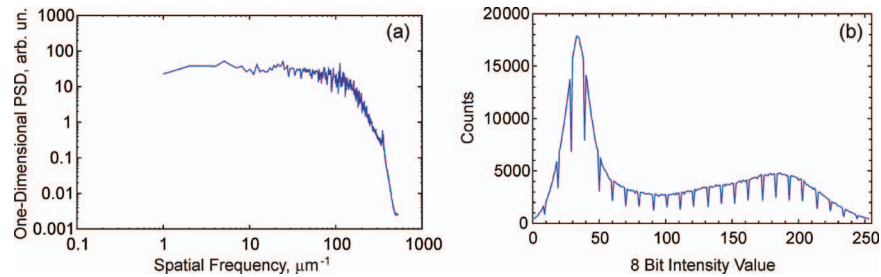


Fig. 8 (a) 1D PSD of the BPRML sample obtained from the average of the PSDs obtained from 6 individual image files as measured with an electron energy of 17.5 keV [Fig. 7(b)]. (b) Histogram of intensity values obtained from a single TEM image measured with 17.5 keV electron energy.

high stability of the measurements allows for effective and reliable stitching of multiple images taken along the sample cross-section. Processing of TEM measurements with stitching will be reported elsewhere. The major conclusion from the presented data is that the TEM measurements testify to the high quality of fabrication of the BPR multilayer with a structure exactly corresponding to the binary sequence that was used.

Similar to the PSD treatment of the SEM images applied in Sec. 4.2, the images in tiff-format obtained with TEM (Fig. 7) were analyzed by converting the image brightness profiles to 1D PSD distributions. Figure 8(a) shows the resulting 1D PSD distribution along the vertical direction of the BPRML sample [Fig. 5(c)] obtained by averaging of six PSDs of the image files measured with 17.5 keV electron energy, as shown in Fig. 7(b).

In the PSD distribution in Fig. 8(a), there is a noticeable spike occurring at about $350 \mu\text{m}^{-1}$. This is most likely due to diffraction related to the nominal 3-nm fundamental layer thickness. In fact, after calibrating the length scale of the images, it was found that the fundamental layer thickness is about 2.8 nm, which would exactly correspond to a diffraction peak at $350 \mu\text{m}^{-1}$. A similar diffraction peak has been observed in scatterometer measurements with a BPR array, when the wavelength of the scattered light was smaller than a fundamental size of the array.³⁷

The PSD measurements with the TEM suggest a number of questions related to a metrological interpretation of the data. One such question is about the high frequency behavior of the PSD spectra in Fig. 8(a). Indeed, because the magnified pixel size is about 1 nm, and the BPRML fundamental thickness is about 3 nm, the TEM measurements are oversampled. In this case, one would expect the high frequency behavior of the PSDs to resemble a Sinc squared function. This is not the case for the spectra shown in Fig. 8(a).

Another question is about the frequency distribution of different intensities in the TEM images recorded with 8-bit resolution. Figure 8(b) shows a histogram of intensity values obtained from a TEM image spread over 2^8 intensity intervals. For the BPR sequence used here, the distribution of the BPRM contrasts (transmissions) should have two equal intensity frequency peaks corresponding to the low and high transmission materials. However, the histogram in Fig. 8(b) demonstrates a significant asymmetry in the appearance of the low and high intensities.

Figure 8(b) illustrates one more problem with TEM data presentation via tiff-files. The surprising (at first glance) spikes in the intensity histogram are probably related to

the well known effect of double compression in the TIFF (MPEG) format.^{65,66}

Therefore, in order to use TEM data for a reliable metrological characterization of a sample under test, one should first address the listed problems. An investigation of these problems and the appropriate way to handle them are currently in progress.

5 Conclusion

We have described a MTF characterization method that is applicable to large aperture optical Fizeau interferometers as well as to scanning and transmission electron microscopes. The used approaches seem to be, at first glance, significantly different. Nevertheless, even in spite of the fact that the instruments are principally different and the MTF test samples developed do not look similar and are made using absolutely different technologies, the basic principle of the MTF calibration method stays the same. That is, the use of the binary pseudorandom test pattern with a deterministic white-noise-like inherent PSD spectrum. Such a correlation between two very distinct applications has demonstrated the deep universality of the calibration method.

Suitable BPR test samples have been fabricated and used for MTF calibration and characterization of a ZygoTM-GPI 6-in. Fizeau interferometer, a NanoLabTM Dual Beam FIB/SEM instrument, and a TecnaiTM transmission electron microscope.

In the case of the optical interferometer, a 2D BPRA test sample of 4027×4029 elements with fundamental element size of $20 \mu\text{m}$ and height of 100 nm fabricated by a conventional microlithography technique was used.

The described MTF measurements with the ZygoTM-GPI have revealed an asymmetry in the measurement along the tangential and sagittal directions. The next step is to fabricate a BPRA test standard on a substrate with high surface flatness. A corresponding analytic model suitable for parameterization of the MTF of an interferometer based on measurements with the BPRA standard should also be developed.

The test samples suitable for calibration of the electron microscopes were made of the BPR multilayer structures with a focused ion beam technique. The BPRM samples of two materials are seen as 1D BPR structures of different contrast when observed with an electron microscope. The fundamental layer thickness of 3 nm and the overall thickness of the multilayer cross-section of about $6 \mu\text{m}$ determine the spatial frequency range available for calibration with the samples.

The preceding SEM measurements with the developed BPRML structure have shown that the SEM images performed at a tilt angle of 52 deg suffer from a limited focus depth of the instrument.

The TEM measurements of the FIB/SEM developed BPRML test samples have confirmed the high quality of the BPR multilayer deposited at NSLS-II. The sharp image contrast between the WSi_2 and Si layers has been demonstrated by super-high resolution measurements with a scanning TEM. We have demonstrated that it is possible to get significant information about metrological reliability of the TEM measurements even for the case when the fundamental frequency of the BPRML sample is smaller by a factor of 1.5 than the Nyquist frequency of the measurements. The measurements bring out a number of problems related to the interpretation of the TEM data.

We plan to develop a BPRML sample consisting of about 4000 layers with an elementary thickness of 1.5 nm. Such a sample would be more suitable for MTF characterization of electron microscopes with higher resolution. We are also working on building an analytical approximation of the measured PSD distributions as they relate to the theoretical PSD inherent to the samples, which would allow us to numerically evaluate the SEM resolution and account for the effect of the defocusing.

In conclusion, the MTF calibration method using BPR test surfaces has significant and universal applicability. It has already been adapted to a number of profiling instruments including interferometric microscopes, scatterometers, interferometers,^{34–39} and, now, large aperture interferometers and scanning and transmission electron microscopes. The existing nanofabrication methods and sample preparation methods, such as FIB sample preparation, are capable of fabricating BPRML test samples suitable for characterization of scanning probe (atomic force) microscopes. The corresponding developments and experiments are in progress at the Advanced Light Source Optical Metrology Laboratory in collaboration with the LBNL Center for X-Ray Optics and the NSLS-II/BNL optics group.

Acknowledgments

The authors are grateful to David Susnitzky, Mark Izquierdo, and Udit Sharma for the FIB/SEM sample preparation and the TEM measurements. The Advanced Light Source is supported by the Director, Office of Science, Office of Basic Energy Sciences, Material Science Division, of the U.S. Department of Energy under Contract No. DE-AC02-05CH11231 at Lawrence Berkeley National Laboratory. Research at Brookhaven National Laboratory is sponsored by the U.S. Department of Energy under Contract No. DE-AC02-98CH10886.

This document was prepared as an account of work sponsored by the United States Government. While this document is believed to contain correct information, neither the United States Government nor any agency thereof, nor The Regents of the University of California, nor any of their employees, makes any warranty, express or implied, or assumes any legal responsibility for the accuracy, completeness, or usefulness of any information, apparatus, product, or process disclosed, or represents that its use would not infringe privately owned rights. Reference herein to any specific commercial product, process, or service by its trade name, trademark, manufac-

turer, or otherwise, does not necessarily constitute or imply its endorsement, recommendation, or favor by the United States Government or any agency thereof, or The Regents of the University of California. The views and opinions of authors expressed herein do not necessarily state or reflect those of the United States Government or any agency thereof or The Regents of the University of California.

References

1. E. L. Church, H. A. Jenkinson, and J. M. Zavada, "Relationship between surface scattering and microtopographic features," *Opt. Eng.* **18**(2), 125–136 (1979).
2. E. L. Church and H. C. Berry, "Spectral analysis of the finish of polished optical surfaces," *Wear* **83**, 189–201 (1982).
3. J. C. Stover, *Optical Scattering*, 2nd Ed., SPIE Optical Engineering Press, Bellingham (1995).
4. D. Attwood, *Soft X-rays and Extreme Ultraviolet Radiation*, Cambridge University Press, New York (1999).
5. Y. Z. Hu and K. Tonder, "Simulation of 3D random rough surface by 2D digital filter and Fourier analysis," *Int. J. Mach. Tools Manufact.* **32**, 83–90 (1992).
6. H. Yamaoka, T. Uruga, E. Arakawa, M. Matsuoka, Y. Ogasaka, K. Yamashita, and N. Ohtomo, "Development and surface evaluation of large SiC x-ray mirrors for high-brilliance synchrotron radiation," *Jpn. J. Appl. Phys.* **33**, 6718–6726 (1994).
7. J. Sherrington and G. W. Howarth, "Approximate numerical models of 3D surface topography generated using sparse frequency domain descriptions," *Int. J. Mach. Tools Manufact.* **38**(5–6), 599–606 (1998).
8. E. Sidick, "Power spectral density specification and analysis of large optical surfaces," *Proc. SPIE* **7390**, 73900L (2009).
9. V. L. Popova and A. É. Filippov, "A model of mechanical polishing in the presence of a lubricant," *Tech. Phys. Lett.* **31**(9), 788–792 (2005).
10. A. V. Pret, R. Gronheid, T. Ishimoto, and K. Sekiguchi, "Resist roughness evaluation and frequency analysis: metrological challenges and potential solutions for extreme ultraviolet lithography," *J. Micro/Nanolith. MEMS MOEMS* **9**(4), 041308 (2010).
11. F. Varnier, N. Mayani, G. Rasigni, and M. Rasigni, "Surface roughness for metallic thin films deposited upon various dielectric coatings," *J. Vac. Sci. Technol. A* **5**(4), 1806–1808 (1987).
12. M. H. Modi, S. K. Rai, M. Thomasset, G. S. Lodha, and M. Idir, "Effect of surface roughness on multilayer film growth," *Eur. Phys. J. Spec. Top.* **167**, 27–32 (2009).
13. G. D. Boreman, *Modulation Transfer Function in Optical and Electro-Optical Systems*, SPIE Press, Bellingham, Washington (2001).
14. K. L. Westra and D. J. Thomson, "Effect of tip shape on surface roughness measurements from atomic force microscopy images of thin films," *J. Vac. Sci. Technol. B* **13**(2), 344–349 (1995).
15. R. N. Bracewell, *The Fourier Transform and Its Applications*, McGraw-Hill Publishing Company, New York (1986).
16. J. M. Elson and J. M. Bennett, "Calculation of the power spectral density from surface profile data," *Appl. Opt.* **34**(1), 201–208 (2001).
17. V. V. Yashchuk, A. D. Franck, S. C. Irick, M. R. Howells, A. A. MacDowell, and W. R. McKinney, "Two dimensional power spectral density measurements of x-ray optics with the MicroMap interferometric microscope," *Proc. SPIE* **5858**, 58580A (2005).
18. V. V. Yashchuk, S. C. Irick, E. M. Gullikson, M. R. Howells, A. A. MacDowell, W. R. McKinney, F. Salmassi, and T. Warwick, "Cross-check of different techniques for two dimensional power spectral density measurements of x-ray optics," *Proc. SPIE* **5921**, 59210G (2005).
19. V. V. Yashchuk, E. M. Gullikson, M. R. Howells, S. C. Irick, A. A. MacDowell, W. R. McKinney, F. Salmassi, T. Warwick, J. P. Metz, and T. W. Tonnessen, "Surface roughness of stainless-steel mirrors for focusing soft x-rays," *Appl. Opt.* **45**(20), 4833–4842 (2006).
20. R. Barakat, "Determination of the optical transfer function directly from the edge spread function," *J. Opt. Soc. Am.* **55**(10), 1217–1219 (1965).
21. B. Tatian, "Method for obtaining the transfer function from the edge response function," *J. Opt. Soc. Am.* **55**(8), 1014–1019 (1965).
22. K. Creath, "Calibration of numerical aperture effects in interferometric microscope objectives," *Appl. Opt.* **28**(15), 3333–3338 (1989).
23. P. Z. Takacs, M. X. Li, K. Furenli, and E. L. Church, "Step-height standard for surface-profiler calibration," *Proc. SPIE* **1995**, 235–244 (1993).
24. A. Harasaki and J. C. Wyant, "Fringe modulation skewing effect in white-light vertical scanning interferometry," *Appl. Opt.* **39**(13), 2101–2106 (2000).
25. G. D. Boreman and S. Yang, "Modulation transfer function measurement using three- and four-bar targets," *Appl. Opt.* **34**(34), 8050–8052 (1995).
26. M. Marchywka and D. G. Socker, "Modulation transfer function measurement technique for small pixel detectors," *Appl. Opt.* **31**(34), 7198–7213 (1992).

27. O. P. Nijhawan, P. K. Datta, and J. Bhushan, "On the measurement of MTF using periodic patterns of rectangular and triangular wave-forms," *Nouv. Rev. Opt.* **6**(1), 33–36 (1975).
28. H. G. Rhee, T. V. Vorburger, J. W. Lee, and J. Fu, "Discrepancies between roughness measurements obtained with phase shifting interferometer and white-light interferometry," *Appl. Opt.* **44**(28), 5919–5927 (2005).
29. J. Chu, Q. Wang, J. P. Lehan, G. Gao, and U. Griesmann, "Measuring the phase transfer function of a phase-shifting interferometer," *Proc. SPIE* **7064**, 70640C (2008).
30. J. Chu, Q. Wang, J. P. Lehan, G. Gao, and U. Griesmann, "Spatially resolved height response of phase-shifting interferometers measured using a patterned mirror with varying spatial frequency," *Opt. Eng.* **49**(9), 095601 (2010).
31. E. Levy, D. Peles, M. Opher-Lipson, and S. G. Lipson, "Modulation transfer function of a lens measured with a random target method," *Appl. Opt.* **38**(4), 679–683 (1999).
32. C. R. Wolfe, J. D. Downie, and J. K. Lawson, "Measuring the spatial frequency transfer function of phase-measuring interferometers for laser optics," *Proc. SPIE* **2870**, 553–557 (1996).
33. J. F. Song and T. Vorburger, "Standard reference specimens in quality control of engineering surfaces," *J. Res. Nation Inst. Stand. Technol.* **96**, 271–289 (1991).
34. V. V. Yashchuk, W. R. McKinney, and P. Z. Takacs, "Binary pseudo-random grating standard for calibration of surface profilometers," *Opt. Eng.* **47**(7), 073602 (2008).
35. V. V. Yashchuk, W. R. McKinney, and P. Z. Takacs, "Binary pseudorandom grating as a standard test surface for measurement of modulation transfer function of interferometric microscopes," *Proc. SPIE* **6704**, 670408 (2007).
36. S. K. Barber, P. Soldate, E. D. Anderson, R. Cambie, W. R. McKinney, P. Z. Takacs, D. L. Voronov, and V. V. Yashchuk, "Development of pseudo-random binary gratings and arrays for calibration of surface profile metrology tools," *J. Vac. Sci. Tech. B* **27**(6), 3213–3219 (2009).
37. S. K. Barber, E. D. Anderson, R. Cambie, W. R. McKinney, P. Z. Takacs, J. C. Stover, D. L. Voronov, and V. V. Yashchuk, "Binary pseudo-random gratings and arrays for calibration of modulation transfer function of surface profilometers," *Nucl. Instr. Meth. A* **616**, 172–182 (2010).
38. S. K. Barber, P. Soldate, E. D. Anderson, R. Cambie, S. Marchesini, W. R. McKinney, P. Z. Takacs, D. L. Voronov, and V. V. Yashchuk, "Binary pseudo-random gratings and arrays for calibration of the modulation transfer function of surface profilometers: recent developments," *Proc. SPIE* **7448**, 744802 (2009).
39. S. K. Barber, E. D. Anderson, R. Cambie, S. Marchesini, W. R. McKinney, P. Z. Takacs, D. L. Voronov, and V. V. Yashchuk, "Stability of modulation transfer function calibration of surface profilometers using binary pseudo-random gratings and arrays with non-ideal groove shapes," *Opt. Eng.* **49**(5), 053606 (2010).
40. P. H. Bardell, W. H. McAnney, and J. Savir, *Built-in Test for VLSI Pseudorandom Techniques*, John Wiley and Sons, Inc., New York (1987).
41. A. Busboom, H. Elders-Boll, and H. D. Schotten, "Uniformly redundant arrays," *Experimental Astronomy. Astrophysical Instrumentation and Methods* **8**, 97–123 (1998).
42. B. Sclar, *Digital Communications: Fundamentals and Applications*, 2nd Ed., Prentice Hall, Englewood Cliffs, NJ (2001).
43. T. Etzon, "Construction for perfect maps and pseudo-random arrays," *IEEE Trans. Inf. Theory* **34**(5), 1308–1316 (1988).
44. D. D. Koleske and S. J. Sibener, "Generation of pseudo-random sequence for use in cross-correlation modulation," *Rev. Sci. Instrum.* **63**(8), 3852–3855 (1992).
45. A. Mitra, "On pseudo-random and orthogonal binary spreading sequences," *International Journal of Information and Communication Engineering* **4**(6), 447–454 (2008).
46. W. T. Chu, "Impulse-response and reverberation-decay measurements made by using a periodic pseudorandom sequence," *Appl. Acoustics* **29**, 193–205 (1990).
47. T. E. Stern, A. Blaquiere, and J. Valat, "Reactivity measurement using pseudo-random source excitation," *J. Nucl. Energy, Parts A/B* **16**, 499–508 (1962).
48. J. Gordon, N. Kroo, G. Orban, L. Pal, P. Pellionisz, F. Szlavik, and I. Vizi, "Correlation type time-of-flight spectrometer with magnetically pulsed polarized neutrons," *Phys. Lett. A* **26**, 122–123 (1968).
49. K. Skold, "A mechanical correlation chopper for thermal neutron spectroscopy," *Nucl. Instrum. Methods* **63**, 114–116 (1968).
50. A. Virjo, "Statistical analysis of cross-correlation chopper for time-of-flight measurements," *Nucl. Instrum. Methods* **63**, 351–352 (1968).
51. A. Virjo, "The Fourier method in slow neutron time-of-flight spectrometry with a pseudo-random input signal," *Nucl. Instrum. Methods* **73**, 189–199 (1969).
52. A. Virjo, "Slow neutron time-of-flight spectrometry with a pseudo-random input signal," *Nucl. Instrum. Methods* **75**(1), 77–84 (1969).
53. V. L. Hirschy and J. P. Aldridge, "A cross correlation chopper for molecular beam modulation," *Rev. Sci. Instrum.* **42**(3), 381–383 (1971).
54. G. Comsa, R. David, and B. J. Schumacher, "Magnetically suspended cross-correlation chopper in molecular beam-surface experiments," *Rev. Sci. Instrum.* **52**(6), 789–791 (1981).
55. V. V. Yashchuk, B. N. Ashkinadzi, M. N. Groshev, V. F. Ezhov, T. A. Isaev, V. A. Knyazkov, G. B. Krygin, and V. L. Ryabov, "Cross-correlation time-of-flight spectrometer of molecular beams," *Instrum. Exp. Tech.* **40**(4), 501–507 (1997).
56. S. M. Kay, *Modern Spectral Estimation: Theory and Application*, Prentice Hall, Englewood Cliffs, New Jersey (1988).
57. E. E. Fenimore and T. M. Cannon, "Coded aperture imaging with uniformly redundant arrays," *Appl. Opt.* **17**(3), 337–347 (1978).
58. E. Caroli, J. B. Stephen, G. Di Cocco, L. Natalucci, and A. Spizzichino, "Coded aperture imaging in x- and gamma-ray astronomy," *Space Sci. Rev.* **45**, 349–403 (1987).
59. E. M. Gullikson, private communication.
60. G. C. Holst, *CCD Arrays, Cameras, and Displays*, SPIE Optical Engineering Press, Bellingham (1998).
61. Materials Science, Inc., <http://www.msi-pse.com/Polaris.htm>.
62. R. Conley, C. Liu, J. Qian, C. M. Kewish, A. T. Macrander, H. Yan, H. C. Kang, J. Maser, and G. B. Stephenson, "Wedged multilayer Laue lens," *Rev. Sci. Instrum.* **79**, 053104 (2008).
63. R. Conley, C. Liu, C. M. Kewish, A. T. Macrander, and C. Morawe, "Multilayer growth in the APS rotary deposition system," *Proc. SPIE* **6704**, 670505 (2007).
64. Evans Analytical Group, Inc., <http://www.eaglabs.com>.
65. W. Wang and H. Farid, "Exposing Digital Forgeries in Video by Detecting Double MPEG Compression," in *MM&Sec2006*, Geneva, Switzerland (2006).
66. A. Popescu and H. Farid, "Statistical tools for digital forensics," in *6th International Workshop on Information Hiding*, Toronto, Canada (2004).



Valeriy V. Yashchuk received his MS degree in experimental physics from St. Petersburg State University (Russia) in 1979, and his PhD degree from St. Petersburg Nuclear Physics Institute (Russia) in 1994. He is currently leading the Optical Metrology Laboratory at the Advanced Light Source, Lawrence Berkeley National Laboratory. He has authored more than 80 scientific articles in the fields of atomic and molecular physics, nonlinear optics, electro- and magneto-optics, laser spectroscopy, experimental scientific methods and instrumentation, and optical metrology. In 1986, for the development of a method of reduction of phase space of an atomic beam, he was awarded the Leningrad Komsomol Prize in Physics. In 2007, he received R&D Magazine's R&D 100 Award for development of a Laser-Detected MRI. His current research interest is in x ray optics, optical instrumentation, and metrology for x ray optics.



Erik H. Anderson attended the Massachusetts Institute of Technology in Cambridge, Massachusetts and received a BS degree in 1981, an MS degree in 1984, and a PhD in 1988, all in the Department of Electrical Engineering and Computer Science. He joined Lawrence Berkeley National Laboratory in 1988 and worked as a visiting scientist at the IBM T. J. Watson Research Laboratory in Yorktown Heights, New York, developing zone plate optics for x ray microscopy. In 1993, he moved to Berkeley to build and manage the nanofabrication facility, within the Center for X-Ray Optics. He is currently involved in EUV and soft x ray optics development, characterization, e-beam lithography, nanofabrication, and x ray microscopy.



Samuel K. Barber received his BS degree in physics from the University of California at Los Angeles in 2007. He joined the Optical Metrology Laboratory at the Advanced Light Source, Lawrence Berkeley National Laboratory in 2008 where he worked on x ray optical instrumentation and metrology. Currently he is pursuing a PhD in physics at the University of California at Los Angeles.



Nathalie Bouet received BS and MPhil degrees from the Department of Chemistry at University of Tours (France) and PhD degree in physics from the University of Orleans (France) in 2006. She has worked for the CNRS at the Centre de Recherche sur la Matiere Divisee and for Boston University in the Physics Department before joining BNL in 2008. Her research interests concern primarily the growth of nanoparticles and films using physical vapor deposition techniques and electron microscopy imaging. At BNL, her efforts have included work on multilayer films growth by sputtering as well as fabrication of Multilayer Laue lenses. She is currently investigating dry etching of multilayered films to produce x ray optics.



Rossana Cambiè received MS and PhD degrees in electrical engineering from the University of Pavia (Italy), finishing in 2003 with a thesis in microelectromechanical system technology and applications in collaboration with ST Microelectronics in Milan, Italy. Rossana has been with the Lawrence Berkeley National Laboratory since 2003 where she provides expertise in micro- and nanofabrication process development and optimization to the Center of Systems Biology Engineering. Her research interests are in instrumentation and metrology for x ray optics and detectors, in-focus phase contrast for electron microscopy, cryo-EM, micro- and nanofluidic systems, and plasmonic applications.



Raymond Conley, after receiving BS and MS degrees in electrical engineering from Northern Illinois University, began his research work in the field of x ray optics fabrication in 2002 at the Advanced Photon Source (APS) at Argonne National Laboratory. While at APS, his research experience was focused primarily on multilayer deposition and thin-film growth. After accepting a position at Brookhaven National Laboratory with the NSLS-II Project, he has managed the construction and technical purpose of a new x ray optics R&D facility. As the optics fabrication group leader, his interests include x ray multilayer deposition and metrology, crystal optics fabrication, and novel methods for x ray optics production.



Wayne R. McKinney received his BA, MA, and PhD degrees in physics from The Johns Hopkins University, finishing in 1974 with a thesis in ultraviolet astronomy. He then completed a post-doctoral appointment in molecular biology supported by a National Cancer Institute Fellowship at the Biology Department of Brookhaven National Laboratory in 1977. Remaining at Brookhaven from 1977 to 1979 in the Instrumentation Division, he designed optical systems for the National Synchrotron Light Source. From 1979 to 1987, he joined the research staff of the Richardson Grating Lab in Rochester New York, becoming manager of Diffraction Grating R&D in 1981. From 1987 to 1989 he was a staff scientist in the Center for X-Ray Optics at Lawrence Berkeley National Laboratory working on water cooled optical components and monochromator designs for the Advanced Light Source. This work won local and national Tech Transfer Awards, and led to fellow status in the OSA. He now works directly for the Advanced Light Source where he designed and built the first infrared beamlines. Currently his responsibilities are in optical metrology, particularly the specification of x ray optics by calculation of scattering.



Peter Z. Takacs directs the activities of the Optical Metrology Laboratory in the Instrumentation Division of Brookhaven National Laboratory. He is actively involved in the development of instrumentation, methods, and standards used for testing the figure and finish of aspheric optics, such as those used for reflecting x rays at grazing incidence. He received a BA degree from Rutgers University in 1969 and a PhD in physics from Johns Hopkins University in 1974. He received an R&D 100 Award and a Photonics Spectra Circle of Excellence Award in 1993 for development of the long trace profiler.



Dmitry L. Voronov received his MS degree in physics of metals and semiconductors from Kharkov Polytechnic Institute in 1989, and his PhD degree from Kharkov National University (Ukraine) in 2003. He is an author of more than 20 publications in the fields of EUV multilayer mirrors, interdiffusion, and phase transformation in metal-silicon thin films. He currently works for the Advanced Light Source, Lawrence Berkeley National Laboratory. His current research is focused on development of high efficiency and high resolution diffraction gratings for EUV and soft x rays.